EUROFUSION WPPFC-PR(16) 14810

TW Morgan et al.

Power handling of a liquid-metal based CPS structure under high heat and particle fluxes

Preprint of Paper to be submitted for publication in
22nd International Conference on Plasma Surface Interactions
in Controlled Fusion Devices (22nd PSI)

This work has been carried out within the framework of the EUROfusion Consortium and has received funding from the Euratom research and training programme 2014-2018 under grant agreement No 633053. The views and opinions expressed herein do not necessarily reflect those of the European Commission.

Power handling of a liquid-metal based CPS structure under high steady-state heat and particle fluxes

T.W Morgan[a,1], A. Vertkov[b], K. Bystrov[a], I. Lyublinski[b], J.W. Genuit[a], G. Mazzitelli[c]

[a]FOM Institute DIFFER – Dutch Institute for Fundamental Energy Research, De Zaale 20, 5612 AJ Eindhoven, the Netherlands

[b]JSC "Red Star", Moscow, Russian Federation

[c]Associazione EURATOM-ENEA sulla fusione, Centro Ricerche di Frascati, Via E. Fermi 45, 00044 Frascati, Italy

Liquid metal infused capillary porous structures (CPSs) are considered as a potential divertor solution for DEMO due to their potential power handling capability and resilience to long term damage. In this work the power handling and performance of such Sn-based CPS systems is assessed both experimentally and via modelling. A Sn-CPS target was exposed to heat fluxes of up to 18.1 MW m-2 in He plasma in the Pilot-PSI linear device. Post-mortem the target showed no damage to nor any surface exposure of the underlying W-CPS felt. The small pore size (~40 µm) employed resulted in no droplet formation from the target in agreement with calculated Rayleigh-Taylor and Kelvin-Helmoholtz instability thresholds. The temperature response of the Sn-target was used to determine the thermal conductivity of the mixed Sn-CPS material using COMSOL modelling. These values were then used via further finite element analysis to extrapolate to DEMO relevant monoblock designs and estimate the maximum power handling achievable based on estimated temperature windows for all component elements of the design. For an optimized design a heat-load of up to 20 MW m-2 may be received while the use of CPS also offers other potential design advantages such as the removal of interlayer requirements.

Keywords: liquid-metal; DEMO; CPS; tin; power-exhaust; plasma-wall interaction

1. Introduction

For DEMO and reactors beyond it, high operational availability and ameliorating neutron-induced effects become much more important as design criteria when considering power exhaust [1]. In particular for the divertor, plasma induced damage, erosion and neutron effects on the plasma facing components (PFCs) will increase irrevocably over time for a solid (W) armour material. This may result in adversely affected plasma performance once a certain damage level is reached, necessitating regular and potentially uneconomical replacement. A liquid plasma-facing surface may help to circumvent these issues, due to its potential for vapour shielding for heat load mitigation, particularly during off-normal or transient effects, self-replenishment following erosion, avoiding net material loss, and avoidance of neutron induced lattice defects and embrittlement.

A question of the potential of liquid metals as PFCs is whether they can lead to an improved exhaust system, permitting a higher or equal heat exhaust than tungsten based DEMO designs, with the added benefit of less frequent replacement or maintenance cycles. Generally three candidate liquid metal materials are currently considered for DEMO: tin (Sn),

[1] Corresponding author: t.w.morgan@differ.nl

lithium (Li) and SnLi eutectic mixtures. Historically Li has been the most widely studied as its use has been shown to improve core performance in many devices [2, 3, 4, 5, 6]. As a divertor material for the PFC its limitations are its high vapour pressure [7] and high hydrogen isotope retention at low temperatures [8]. These may severely limit the operating temperature window between maintaining a low retained hydrogen fraction and a tolerable evaporation rate, limiting the power handling potential. Sn has a much lower vapour pressure and its retention rate for deuterium was recently measured a <0.1% [9]. Due to its high-Z nature only small amounts can be tolerated in the core plasma, but it may offer a much wider operating temperature range and thus potentially higher power handling, and so was assessed here.

2. Methodology

2.1 Sample preparation

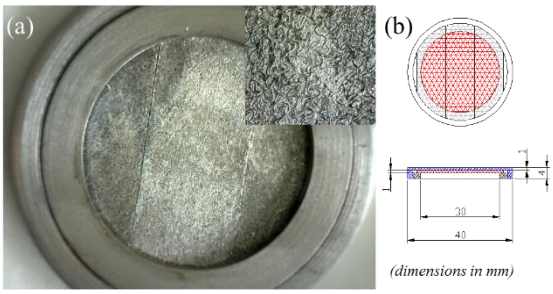

Figure 1: (a) the Sn-target prior to exposure in Pilot-PSI. Inset: Microscope enlargement of the wetted W-felt filled with Sn-CPS. (b) The dimensions of Sn-target showing the Sn-filled CPS (red hashes), Mo cup (blue hashes) and Mo locking ring (black hashes).

The sample (Sn-target) consisted of a 1 mm thick, Sn impregnated CPS tungsten felt in a Mo cup (**Error! Reference source not found.**). The CPS structure consisted of pressed W wire, or so called metallic felt, as previously used in [10]. The wire diameter was 50 µm with a pore diameter of 30-50 µm, giving an open porosity of ~40%. Chemically cleaned strips of the W felt were exposed in a Sn pool at a temperature of 1500 °C for one hour under vacuum conditions. This lead to good wetting, with wetting angle below 30°. Due to this the structure was completely filled in the volume fraction $f = V_{Sn}/(V_{Sn}+V_W)$ = 0.4. This was confirmed via gravimetric analysis.

Following the wetting procedure the strips were placed in the Mo cup and fixed with a Mo locking ring. The fully assembled sample was heat treated at 1000 °C in vacuum to ensure a good wetting of the Mo cup, enabling good heat contact between the CPS and the cup as a result.

For comparison discharges a solid rolled W sample (W-target) made by Advanced Technology & Materials CO., Ltd. (China) was used. This sample was 3.3 mm thick and 30 mm in diameter and was ground to present a smooth surface to the plasma and rear cooling.

2.2 Experimental details

A series of increasing power He plasma discharges were carried out in the linear plasma device Pilot-PSI [11, 12] on both the Sn-target and the W-target. Both samples in turn were mounted using a Mo clamping ring to a water cooled copper plate, with a thickness from surface to cooling water of 4 mm. Between the target and the copper surface a 0.5 mm thick layer of grafoil [13] was used to provide good thermal connection.

The front face target temperature was determined using an infra-red (IR) camera (FLIR SC7500MB, 50 Hz) in combination with a multi-wavelength spectro-pyrometer (FAR Associates FMPI) which gave an emissivity independent temperature at the target centre (r~ 0-0.5 mm) for temperatures >650 °C. Viewing tangentially to the target a fast visible camera

(Phantom V12) was employed to monitor Sn neutral density in the plasma from the 452.5 nm emission line as well as macroscopic (e.g. droplet) emission. A survey spectrometer (Avantes ULS2048) with spot diameter ~ 1 mm centred at $r = 0$ was used to monitor emission in the range 299-579 nm viewing at an angle of ~15° to normal. The total absorbed energy was recorded using cooling water calorimetry. As the visible camera occupied the same port as the Thomson scattering (TS) diagnostic during the Sn-target discharges, TS was used to determine electron density (n_e) and temperature (T_e) and thus particle flux (Γ) and heat flux density (q) only on the W-target discharges. The plasma beam had a Gaussian cross-sectional shape with full-width half-maximum ~15 mm. All values referred to are the maximal value at the centre of the plasma beam ($r = 0$).

Each sample was exposed to an identical set of discharges of increasing q and Γ in the range 1.8-20 MW m^{-2} and 1.5-6.0·10^{24} m^{-2} s^{-1}. This equates to an electron temperature and density range of 1.1-3.7 eV and 1.5-7.0·10^{24} m^{-3} respectively. Each discharge time (t) was 10 seconds in duration, more than sufficient for thermal equilibrium to be reached. No bias was applied and the targets were at floating potential.

Post-mortem analysis was carried out using optical microscopy (Dino-lite Pro AM4113T) and X-ray photoelectron spectroscopy (XPS- ThermoFisher Scientific K-alpha).

3. Results and discussion

3.1 Post-mortem surface analysis

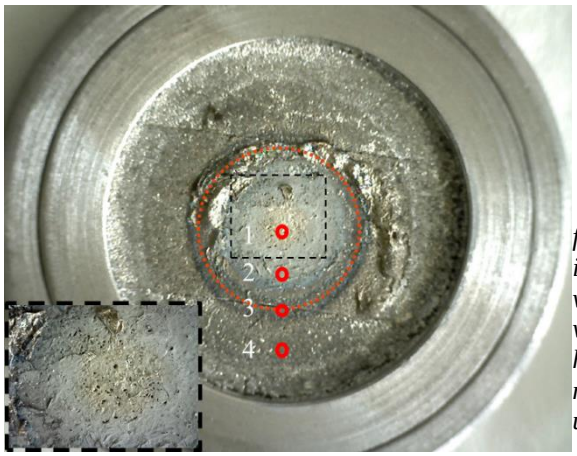

Figure 2: The surface of the Sn-target following the plasma exposure. The dashed red line indicates the approximate extent of the plasma beam while the black dashed box shows the central region which is enlarged (inset), showing the region where holes in the surface have appeared. The four numbered circles indicate the positions investigated using XPS.

Error! Reference source not found. shows the surface of the Sn-target following the series of plasma discharges described above. At the beam centre holes in the Sn-filling can be observed indicating erosion or displacement of tin from this region (**Error! Reference source not found.** inset). Despite this however no damage to the W-felt structure is apparent. A broken ring of loose surface tin is located at the edge of the plasma-wetted region. In IR videos at the highest powers and high temperatures (>1000 °C) this loose surface tin was observed to rotate on the surface. This rotation is driven by **j**x**B** forces, where a radial return current is driven in the target by the plasma density profile [14, 15]. Analogous to how debris can act in a whirlpool, outside of the beam wetted region this force does not act and so tin collects in this region. As the pore size is small enough to confine the tin inside the CPS against hydrostatic pressure (see section 3.2) this surface tin is attributed to the volume expansion of the tin at high temperatures. At 1000 °C the specific volume of Sn increases to 0.155 cm^3 g^{-1} compared to

0.143 cm^3 g^{-1} at 230 °C [16], thus increasing the volume of Sn by ~16 mm^3, approximately equal to the amount of tin observed post-mortem: ~24±12 mm^3.

Position	Sn	O	N	C	Mn	other
1	7.89	36.11	13.45	27.79	5.47	9.29
2	16.88	36.45	11.03	30.29	5.35	0
3	3.16	48.71	15.28	19.35	6.29	7.21
4	3.4	36.7	11.8	30.94	5.96	11.2

Table 1: Elemental At% identified by XPS at four positions indicated in Figure 2

The elemental composition of the surface (0-10 nm) was determined using XPS at four positions with spot size 200 µm as shown in **Error! Reference source not found.**. All positions show quite similar composition (**Error! Reference source not found.**). Notably Sn, oxides and nitrides as well as C (from adventitious carbon contamination in atmosphere) is observed. No tungsten was observed at any position, despite its use as a CPS material, which indicates that despite the plasma exposure, erosion and melt motion, the CPS remains wetted. The origin of the manganese observed, including at position 4 outside the plasma wetted region, is unknown but is possibly due to evaporation from stainless steel [17].

3.2 Stability analysis

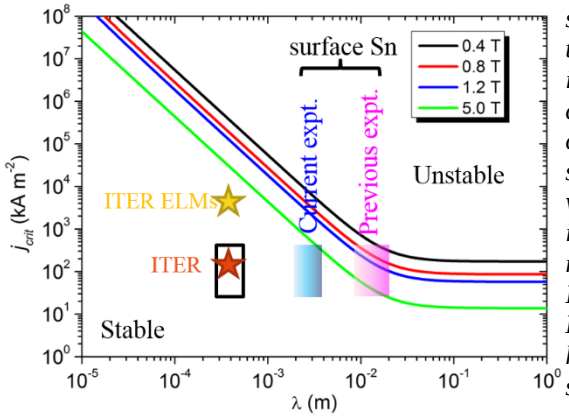

Figure 3: Critical current to drive jxB initiated Rayleigh-Taylor instabilities at the liquid surface as a function of characteristic wavelength (λ). The lines give the stability boundary for the different magnetic field strengths used in Pilot-PSI (0.4-1.2 T) as well as the 5 T expected on-axis magnetic field strength in ITER. The black box shows the range of currents and wavelengths present for Sn confined in pores, while the blue and pink shaded edges give the maximum characteristic wavelength and current range for the surface tin in current and previous experiments **[18]** *respectively. Expected currents for Sn in ITER-like conditions during steady state and ELMs are also marked for the pore sizes used here, indicating they would lie below the stability boundary.*

During the plasma exposure no droplets were observed on either visible or IR camera, in contrast to earlier experiments [18]. This is attributed to the much smaller effective pore size used here (~40 µm) such that the Laplace pressure due to the CPS is much greater than the hydrostatic pressure. In the present case the ratio is approximately 15:1 compared to 2.5÷0.5:1 previously (~200-800 µm pore size). These lower values lead to accumulation of a large amount of unbound Sn on the CPS surface, collecting via gravity at the lower half of the cup. An analysis for Rayleigh-Taylor stability was recently reported [19, 20] and was followed here

for Sn in Pilot-PSI conditions (**Error! Reference source not found.**). The destabilization of the liquid into the plasma is driven the **j**x**B** forces where **j** is in this case the radial target current, while the stability depends on the critical wavelengths which can be supported (λ) with the lowest critical current (j_{crit}). For confined Sn λ=30-50 µm due to the restrictions from the pores, while for the loose tin in these experiments λ<5 mm due to the small islands of surface tin, both of which lies below j_{crit}. In the previous experiments λ<20 mm which crosses the stability threshold, thus leading to droplet production. The expected stability of Sn in ITER-like conditions can also be estimated with ~5 T toroidal field at the divertor position, assuming critical currents of ~100 kA m^{-2} and 5000 kA m^{-2} for steady-state and ELMing conditions respectively. Despite the higher **j**x**B** driving forces and lower stability boundary Sn in pores of similar size as here would remain stable.

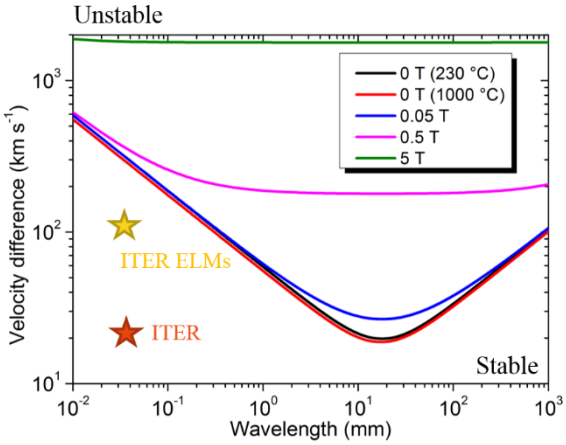

Figure 4: Critical velocity difference to drive Kelvin-Helmholtz instabilities at the liquid surface as a function of characteristic wavelength. The lines give the stability boundaries for different magnetic field strengths. Expected velocity differences for Sn in ITER-like conditions during steady state and ELMs are also marked for the pore sizes used here, indicating they would lie below the stability boundary.

An analysis of vulnerability to Kelvin-Helmholtz instabilities can also be made for Sn CPS, this time by substituting for W melt motion with Sn properties following [21] (**Error! Reference source not found.**). The rotation of the plasma column in Pilot-PSI would be the driving force in this case [22]. This rotation has been previously determined for H-plasma under similar conditions as maximally 8000 m s^{-1} [22]. Therefore even unbound surface Sn is stable. In ITER the plasma flow is strongest toroidally, but this direction is strongly additionally stabilized by the magnetic field in that direction. Assuming maximally flow at the sound speed near the target surface and a plasma density of 10^{21} m^{-3} we can estimate that the Sn surface is again stable for similar pore sizes both for ITER-like steady-state (D-ions, T_e = 5 eV) and maximal type-I ELMing loads (D-ions, T_e ~4.5 keV), even without accounting for additional magnetic stabilization.

3.3 Thermal response

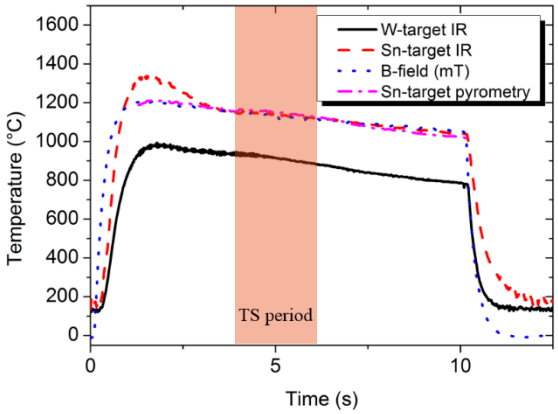

Figure 5: Surface temperature evolution with time at r=0 determined by the IR camera or determined by pyrometry. The magnetic field strength evolution is also shown, as well as the recording period of the TS system.

Error! Reference source not found. shows an example, each at q = 18.1 MW m^{-2}, of the surface temperature evolution that was observed for the Sn-target and W-target cases in the IR data at r = 0. In the W-target cases a sharp ramp in temperature reaches equilibrium within t = 1-3 seconds and then shows a gradual decrease in temperature over the duration of the shot from the maximum value. This is related to a corresponding decrease in magnetic field strength over the duration of the discharge due to the slow Ohmic heating and increasing resistance of the coils with time. The decrease rate was ~0.01B s^{-1} with correspondingly decreasing values seen in the temperature data. For the Sn-target case an additional temperature rise is observed in the first 1-3 seconds of the shot on top of this, which then swiftly decreases and reaches an equilibrium value by around t = 4-5 seconds which then shows a similar decline as in the W-target cases. Because this effect was not observed in the pyrometry data we attribute it to changing surface emissivity caused by the phase change from solid to liquid and the removal of impurities from the surface by the plasma.

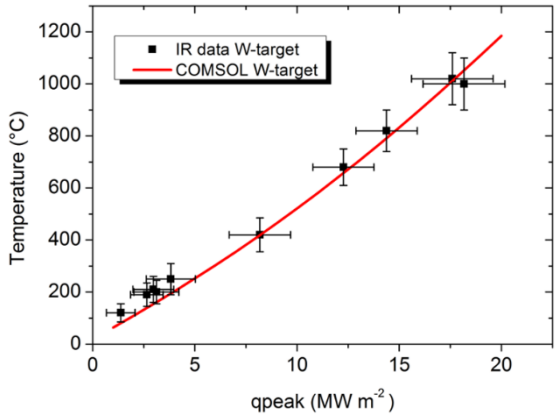

Figure 6: Equilibrium temperature values at r = 0 as a function of q for the W-target compared to a COMSOL model of the equilibrium temperatures.

Error! Reference source not found. shows the central (r=0) equilibrium temperature reached as a function of the central power density q_0 of the W-target. The TS data used to derive q_0 was recorded between t = 4-6 s, so due to the decay in magnetic field strength the average peak temperature during the equilibrium period for the duration t = 4-6 s was used and the variation incorporated into the error determination. The TS data was only recorded during the W-target discharges and therefore calorimetry data, which is also proportional to the applied heat flux was used to confirm that power loading was the same in both cases.

The observed temperature rise of the W-target was compared to a finite element (FE: COMSOL Multiphysics 5.1) model of the equilibrium surface temperature at the same position when an identical Gaussian heat load was applied. The 3D model replicates the dimensions of

the target assembly and the temperature dependent thermal conductivities (k) of the constituent parts (copper base plate [23], grafoil layer [13], Mo clamping ring [24] and W target [23]) were incorporated. This forward model is also shown in **Error! Reference source not found.** and shows excellent agreement within the error bars. This therefore validates the model when assessing the performance of the Sn-target.

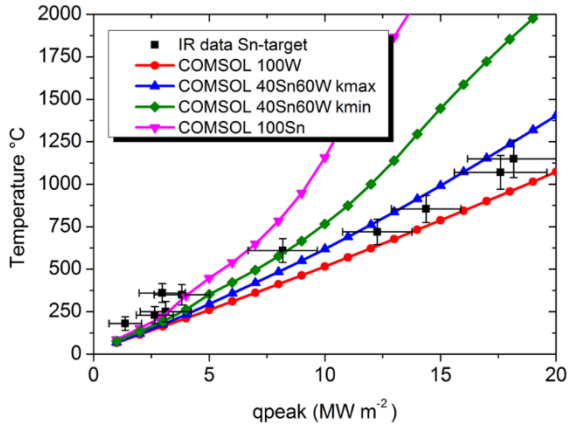

Figure 7: Equilibrium temperature values at r = 0 as a function of q for the Sn- compared to four COMSOL models treating the CPS layer thermally as pure W/pure Sn or a mixed material with maximal/minimal thermal conductivity.

Error! Reference source not found. shows the central equilibrium temperature of the Sn-target as a function of q_0 as well as four possible COMSOL models of the equilibrium temperature, treating the CPS mixed layer in four possible ways. These are to treat the thermal conductivity of the CPS layer as pure Sn (with thermal conductivity as given in [25]), pure W or as a mixture. Using the rule of mixtures k_{CPS} can lie between the values

$$\left(\frac{f}{k_{Sn}}+\frac{1-f}{k_W}\right)^{-1} \leq k_{CPS} \leq f k_{Sn} + (1-f)k_W \qquad (1)$$

Where k_i is the thermal conductivity of material i. The two extreme cases are also shown in the figure. From the observed results clearly the right hand side of the inequality in (1) is the most appropriate to use to describe the mixed CPS thermal conductivity and is used below.

3.4 COMSOL monoblock modelling

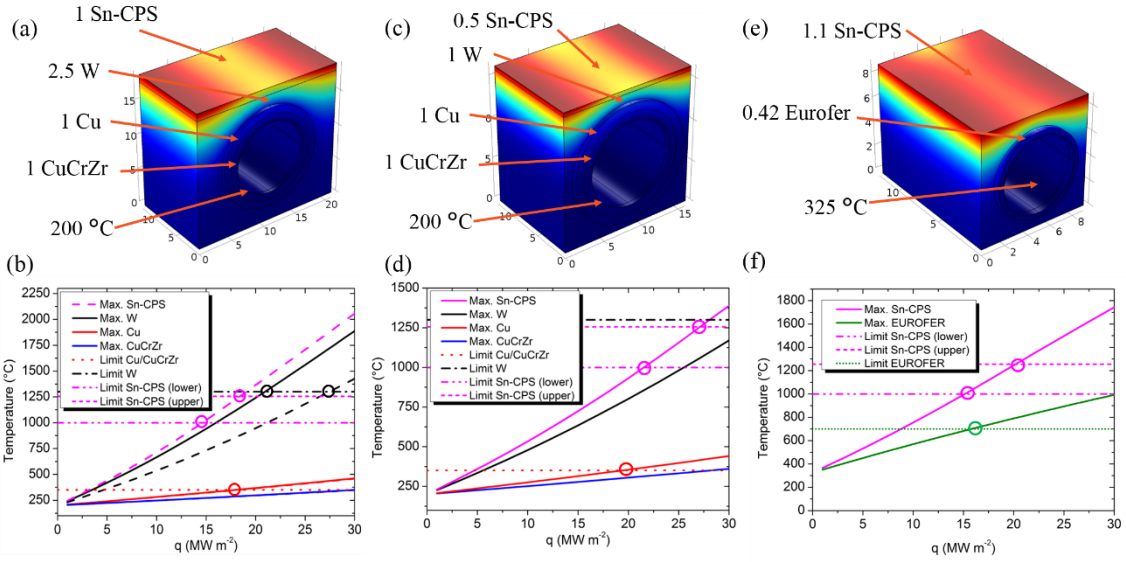

Figure 8: Dimensions of COMSOL models of monoblock designs for (a) replacement of top 1 mm with Sn-CPS (c) optimized CPS layer design and (e) fully CPS monoblock with steel tube and no interlayer. In figures (b), (d) and (f) for these respective designs, the maximum equilibrium temperature as a function of heat load applied uniformly on the top surface, as well as the material temperature limits is shown for Sn-CPS, W, Cu, CuCrZr and Eurofer, while the intersection of these limits with the expected temperature is identified with circles of the relevant colour.

Given we can model k_{CPS} using the rule of mixtures it is possible to assess how a Sn-CPS structure would perform as a DEMO divertor option. Recent work on a CuCrZr "improved" concept (figure 2 [26]) on optimizing a tungsten-monoblock based design for ITER was used as the basis for the model here. The dimensions and coolant (water at 200 °C) were kept as in [26] except that the top 1 mm of the surface was replaced with a Sn-CPS layer (**Error! Reference source not found.**(a)). Such a layer could be supplied with Sn using the spacing between the monoblocks as a wicking region as proposed for the NSTX refilling divertor [27]. A uniform heat load q was applied at the top surface and the maximum equilibrium temperature determined in the range 1-30 MW m^{-2}. Temperature dependent thermal conductivities as in section 3.3 were used, identical to those in [26] with $k_{CPS} \sim f k_{Sn} + (1-f)k_W$. The maximum heat load that can be sustained was determined from the temperature limits of the constituent components of the monoblock. For Cu and its alloys the temperature window for high heat transfer without mechanical damage is limited by neutron loading to the range 200-350 °C [26] while for W the limitation is given by recrystallization to <1300 °C [28]. For Sn the temperature limit should be such to limit the evaporation to an acceptable level that core performance is not affected. No reliable model exists to predict what this level should be, but conservative estimations give an evaporation rate of 10^{20} m^{-2} s^{-1} or more optimistically 10^{22} m^{-2} s^{-1} to avoid intolerable core radiation [7]. Evaporation rates can be determined from Langmuir's law [29] and the empirically determined evaporation pressure of Sn and give temperature limits of ~1000 °C or ~1250 °C respectively [7]. In this case the lower limit (1000 °C) this would be the limiting factor but for the upper limit (1250 °C) the limit would be given by the temperature window of the copper interlayer used, identical to in the case without a CPS layer (**Error! Reference source not found.**(b)). Overall the maximum heat load performance would be slightly decreased from 18 MW m^{-2} to 15 MW m^{-2}, but with the benefit of a replenishing CPS layer.

Considering the refilling characteristics of such a layer such that an ablative armour layer is unneccesary, we can consider further reduction in the dimensions of the W monoblock layer, as shown in **Error! Reference source not found.**(c). Thus the W thickness is reduced to 1 mm and the CPS to 0.5 mm thick, while maintain the same dimensions for the CuCrZr pipe and interlayer and the same coolant and coolant temperature. In such a case the heat load window could be increased to 20 MW m^{-2} (**Error! Reference source not found.**(d)), this time limited by the Cu interlayer temperature window (for the Sn-CPS layer the limit is approximately 23 MW m^{-2}).

We can also consider replacing all solid W in the monoblock with Sn-CPS. This would provide the benefit of removing the need for an interlayer against interface stress due to the flexible nature of the CPS during thermal expansion. This could be beneficial in permitting steel (e.g. Eurofer) pipes to be used, where there are not many suitable interlayer materials readily available [30]. Also, all clamped, large solid W pieces are removed from the design and replaced with a W mesh impregrated with Sn. This therefore reduces the risks associated with fatigue cracking to the pipe and a loss-of-coolant accident, or the self castellations recently observed in some ITER divertor mock-ups under heat load testing [31]. All W is in wire form

which will act in a more ductile manner than a bulk substance, while any eventual fatigue or thermal cracking of the mesh will be localized to individual wires each time.
Such a case is addressed in **Error! Reference source not found.**(e). The model is now based on a Eurofer improved concept (figure 3 [26]) in terms of steel pipe diameter and thickness and the water coolant temperature is set to 325 °C. The copper interlayer however is removed and the monoblock is made from Sn CPS mesh and considerably thinned. The thermal conductivity of 660 stainless steel was used [23]. **Error! Reference source not found.**(f) shows that such a design could sustain up to 15 MW m^{-2}.
It should be noted that, as in other work of this type, thermal conductivities used were for unirradiated materials, whereas neutron loading will lead to a decrease in thermal conductivity of the solid components [28]. Therefore these numbers would likely represent an upper limit and decrease following sufficient neutron exposure. Secondly, while effort was made to choose pipe and block dimensions which have been stress analysed [26], and thus retain a configuration which would remain within tolerable limits, no dedicated FE stress analysis was carried out. This would be eventually needed to further ensure that the designs suggested here reach engineering requirements.

Conclusions

In this paper the power handling capability of liquid Sn in a CPS system is assessed, as well as its overall resilience and stability, under high thermal and particle loads. Exposures in the Pilot-PSI linear device demonstrated that a Sn-CPS target can receive up to 18 MW m^{-2} without apparent damage to the underlying W wire felt, and XPS results indicate that the CPS remains wetted by the Sn following exposure. The sample demonstrated no macroscopic erosion, i.e. droplet formation is observed. This was associated with the much smaller pore size and higher surface tension forces providing capillary restraint in this work compared to previous experiments with larger pore size. Lack of droplet production and droplet production in previous experiments was in agreement with stability analysis of Rayleigh-Taylor and Kelvin-Helmholtz instabilities. These assessments also indicate that CPS restrained Sn would remain below the limit for instability growth under ITER-like steady-state as well as ELMing conditions.

A thermal analysis of the target assembly indicated that the thermal conductivity of the Sn-CPS can be best represented as $k_{CPS} \sim f k_{Sn} + (1-f)k_W$ based on the rule of mixtures. Using this the effect of adding a CPS layer was determined for a DEMO monoblock configuration using finite element (COMSOL) analysis and found to lead to a small reduction in maximum power load from 18 MW m^{-2} to 15 MW m^{-2} in an un-optimized case to remain below a limit on the evaporation rate of 10^{20} m^{-2} s^{-1} to maintain good core compatibility. When shrinking the monoblock to optimize the armour thickness further a heat load of 20 MW m^{-2} may be sustained, thus giving a higher performance than without the CPS layer. A case where the entire solid W armour was replaced with Sn-CPS, thus permitting a higher coolant temperature of 325 °C and steel cooling pipe without interlayer, was also considered. In this case a maximum heat load of 15 MW m^{-2} was estimated. Overall therefore these results indicate that Sn-CPS can be an effective as part of a plasma facing component, giving equal or greater power handling capability, while retaining the inherent advantages of liquid metal deployment in the DEMO divertor over fully solid structures. Further analysis and modelling, as well as loading of such components under realistic power and particle loading, should be a focus for future work in this area.

Acknowledgements

This project was carried out with financial support from NWO. The work has been carried out within the framework of the EUROfusion Consortium and has received funding from the Euratom research and training programme 2014-2018 under grant agreement No 633053. The views and opinions expressed herein do not necessarily reflect those of the European Commission.

References

D. Stork et al. Fus. Eng. Des. 89 (2014) 1586-1594.
1]

G. Mazzitelli et al. Fus. Eng. Des. 85 (2010) 896-901.
2]

S.V. Mirnov, E.A. Azizov, V.A. Evtikhin, V.B. Lazarev and I.E. Lyublinski
3] Plasma Phys. Control. Fusion 48 (2006) 821–837.

M. Ono et al. Nucl. Fusion 53 (2013) 113030.
4]

D. K. Mansfield et al. Phys. Plasmas 3 (1996) 1892.
5]

R. Majeski et. al Fus. Eng. Des. 65 (2003) 443-447.
6]

J.W. Coenen et al. Phys. Scr. T159 (2014) 014037.
7]

M.J. Baldwin, R.P. Doerner, S.C. Luckhardt, and R.W. Conn Nucl. Fusion 42
8] (2002) 1318-1323.

J.P.S. Loureiro et al. (2016) (submitted to Nucl. Mater. Energ).
9]

G. Mazzitelli et al. J. Nucl. Mater. 463 (2015) 1152-1155.
10]

G. J. van Rooij et al. Appl. Phys. Lett. 90 (2007) 121501.
11]

G. De Temmerman, J.J. Zielinski, S. van Diepen, L.Marot and M. Price Nucl.
12] Fusion 51 (2011) 073008.

Grafoil Engineering Manual 2nd Ed. (01-06-2016)
13] (http://www.graftech.com/wp-content/uploads/2014/12/GRAFOIL-Engineering-Manual-2nd-Ed.pdf).

A E Shumack, H J de Blank, J Westerhout and G J van Rooij Plasma Phys. Control.
14] Fusion 54 (2012) 125006.

G. De Temmerman, J. Daniels, K. Bystrov, M.A. van den Berg and J.J. Zielinski
15] Nucl. Fusion 53 (2013) 023008.

S. Sharafat and N. Ghoniem Apex report UCLA-UCMEP-00-31 (2000).
16]

D.T. Bourgette ORNL Report 3677 'Evaporation of iron- nickel- and cobalt-base

17] alloys at 760-980 C in high vacuums (1964).

T.W. Morgan, D.C.M. van den Bekerom and G. De Temmerman J. Nucl. Mater.
18] 463 (2015) 1256–1259.

M.A. Jaworski et al. Nucl. Fusion 53 (2013) 083032.
19]

M A Jaworski, A Khodak and R Kaita Plasma Phys. Control. Fusion 55 (2013)
20] 124040.

G.V. Miloshevsky and A. Hassanein Nucl. Fusion 50 (2010) 115005.
21]

A. E. Shumack et al. Phys. Rev. E 78 (2008) 046405.
22]

ITER Materials Properties Handbook v3.3 G 74 MA 8 01-05-28 W 0.2 (2013)
23] (internal project document distributed to the ITER Participants).

Plansee Ltd (01-06-2016)
24] (http://www.plansee.com/en/materials/molybdenum.html).

E. Yamasue, M. Susa, H. Fukuyama, K. Nagata Int. J. Thermophys. 3 (2003)
25] 713-730.

A. Li-Puma et al. Fus. Eng. Des. 88 (2013) 1836-1843.
26]

P. Rindt et al. submitted to Fusion Eng. Des. (2016).
27]

V. Barabash, G. Federici, J. Linke and C.H. Wu J. Nucl. Mater. 313–316 (2003)
28] 42–51.

I. Langmuir, Proc. Natl. Acad. Sci. U.S.A. 45 (1917) 452.
29]

L. Giancarli et al. Fus. Eng. Des. 75-79 (2005) 383-386.
30]

T. Hirai et al. J. Nucl. Mater. 463 (2015) 1248-1251.
31]